

Partitioning CloudSat ice water content for comparison with upper tropospheric ice in global atmospheric models

Wei-Ting Chen,¹ Christopher P. Woods,^{1,2} Jui-Lin F. Li,¹ Duane E. Waliser,¹ Jiun-Dar Chern,³ Wei-Kuo Tao,³ Jonathan H. Jiang,¹ and Adrian M. Tompkins^{4,5}

Received 11 October 2010; revised 12 July 2011; accepted 19 July 2011; published 12 October 2011.

[1] The ice cloud estimates in current global models exhibit significant inconsistency, resulting in a significant amount of uncertainties in climate forecasting. Vertically resolved ice water content (IWC) is recently available from new satellite products, such as CloudSat, providing important observational constraints for evaluating the global models. To account for the varied nature of the model parameterization schemes, it is valuable to develop methods to distinguish the cloud versus precipitating ice components from the remotely sensed estimates in order to carry out meaningful model-data comparisons. The present study develops a new technique that partitions CloudSat total IWC into small and large ice hydrometeors, using the ice particle size distribution (PSD) parameters provided by the retrieval algorithm. The global statistics of CloudSat-retrieved PSD are analyzed for the filtered subsets on the basis of convection and precipitation flags to identify appropriate particle size separation. Results are compared with previous partitioning estimates and suggest that the small particles contribute to ~25–45% of the global mean total IWC in the upper to middle troposphere. Sensitivity measures with respect to the PSD parameters and the retrieval algorithm are presented. The current estimates are applied to evaluate the IWC estimates from the European Centre for Medium-Range Weather Forecasts model and the finite-volume multiscale modeling framework model, pointing to specific areas of potential model improvements. These results are discussed in terms of applications to model diagnostics, providing implications for reducing the uncertainty in the model representation of cloud feedback and precipitation.

Citation: Chen, W.-T., C. P. Woods, J.-L. F. Li, D. E. Waliser, J.-D. Chern, W.-K. Tao, J. H. Jiang, and A. M. Tompkins (2011), Partitioning CloudSat ice water content for comparison with upper tropospheric ice in global atmospheric models, *J. Geophys. Res.*, 116, D19206, doi:10.1029/2010JD015179.

1. Introduction

[2] Ice clouds are an important modulator of the climate system [Lynch *et al.*, 2002; Ramanathan and Collins, 1991; Stephens, 2005]. They significantly contribute to the radiation budget through both their shortwave albedo effects and long-wave greenhouse effects [Chen *et al.*, 2000; Comstock *et al.*, 2002; Hartmann and Short, 1980; Liou, 1976; McFarquhar *et al.*, 2000; Ramanathan *et al.*, 1989; Ramanathan and Collins, 1991; Randall and Tjemkes, 1991]. Their generation and dissipation is closely connected to the hydrological cycles through associated processes, such as convection, latent

heating, and precipitation [e.g., Baker, 1997; Del Genio and Kovari, 2002; Kahn *et al.*, 2008; Krueger *et al.*, 1995; Lilly, 1988; Kärcher and Ström, 2003; Luo and Rossow, 2004; Rossow and Schiffer, 1999]. Given their large radiative impacts, subtle variations of the spatial distribution, height, frequency of occurrence, thickness, and optical and microphysical properties of the ice clouds can cause substantial feedbacks to the climate [Fu and Liou, 1992; Hartmann and Doelling, 1991; Hartmann *et al.*, 1992; Kiehl, 1994; Miller, 1997; Stephens *et al.*, 1981; Zelinka and Hartmann, 2010]. Accurate characterizations of these properties are therefore crucial to understand the ice clouds' climatic influences, as well as their responses in a changing climate.

[3] Climate sensitivity estimate for most models depends critically on the representation of clouds. It is very evident that large disagreement exists in the ice clouds represented in general circulation models (GCMs) [Li *et al.*, 2005, 2007; Waliser *et al.*, 2009]. This is illustrated in Figure 1 by the annual mean ice water path (IWP) estimates from fourteen GCMs contributing to the Intergovernmental Panel on Climate Change Fourth Assessment Report (IPCC AR4). The differences can

¹Jet Propulsion Laboratory, California Institute of Technology, Pasadena, California, USA.

²Now at Aerospace Corporation, El Segundo, California, USA.

³NASA Goddard Space Flight Center, Greenbelt, Maryland, USA.

⁴European Centre for Medium-Range Weather Forecasts, Reading, UK.

⁵Also at Abdus Salam International Centre for Theoretical Physics, Trieste, Italy.

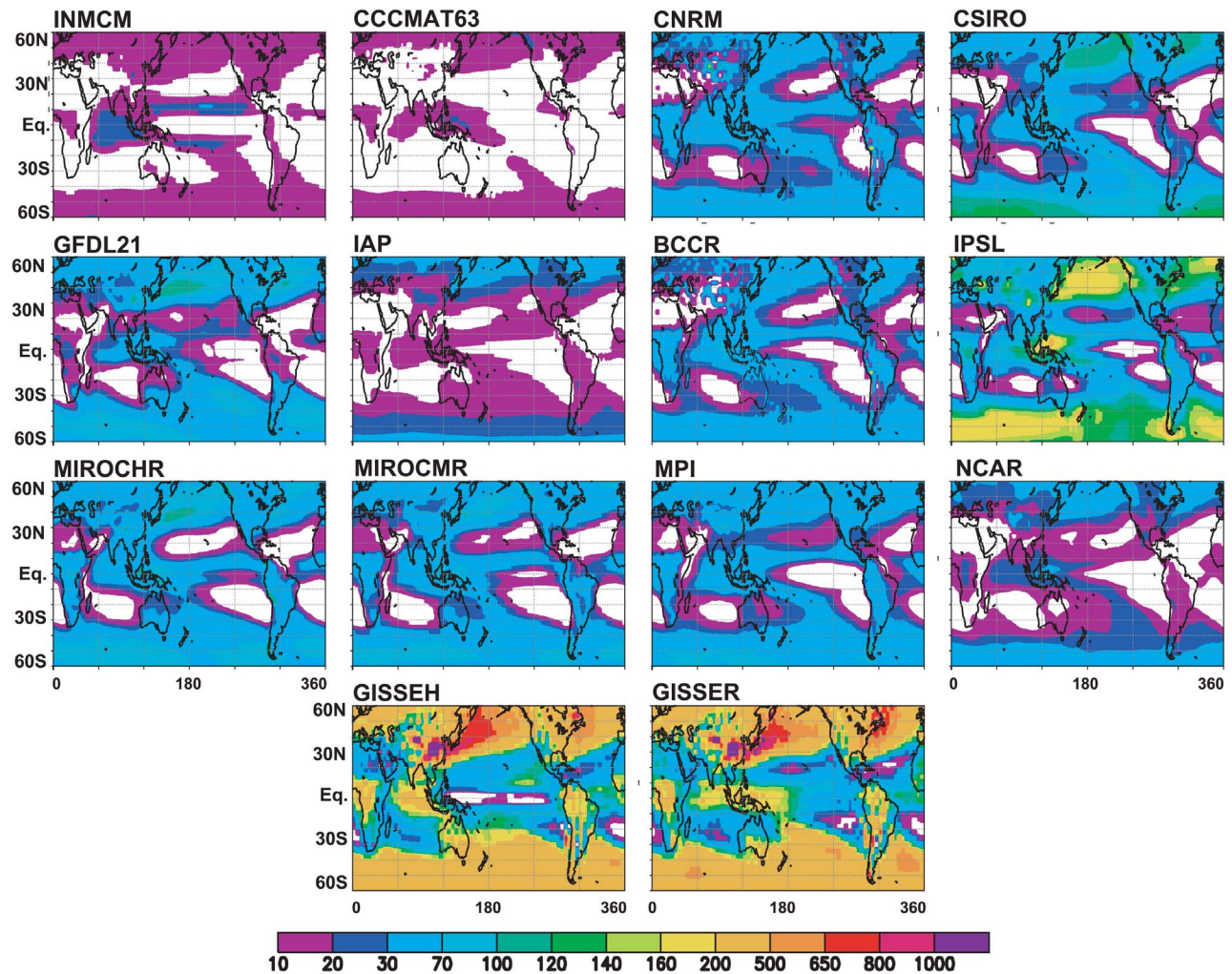


Figure 1. Global maps of annual mean ice water path (in g m^{-2}) in the 1970–1994 period from the 20th century simulations (scenario 20c3m) in the 14 GCMs contributing to IPCC AR4 (modified from *Waliser et al. [2009]*).

be nearly two orders of magnitude in some regions, and even for globally averaged values the disagreement between the lowest and highest model estimates can be a factor of 20 [*Waliser et al., 2009*]. It is imperative to reduce such levels of model uncertainty and bias for a quantity as fundamental and conceptually unambiguous as atmospheric ice mass, especially for the models that will provide future climate projections for the next IPCC assessment report.

[4] Efforts have been made to derive robust global observational constraints to facilitate the evaluation and improvement of the ice cloud representations in global models. The most recent and valuable additions to the observational resources are the vertically resolved ice cloud water content (IWC) retrieval estimates from radar/lidar/limb sounding, such as those from the CloudSat, the Cloud-Aerosol Lidar Infrared Pathfinder Satellite Observations (CALIPSO), and the Microwave Limb Sounder (MLS). These new satellite products represent a great leap forward in ice cloud observation, as the in situ measurements offer only sparse sampling [e.g., *McFarquhar and Heymsfield, 1996; McFarquhar et al., 2000*], and the global retrievals from passive nadir-viewing sensors (especially those using

infrared, visible, and UV techniques) can exhibit large uncertainty when probing thick clouds with precipitation, mixed phased hydrometeors, and/or multilayer structures [*Lin and Rossow, 1996; Stephens et al., 2002; Wu et al., 2006*]. Although these data sets have proven beneficial in model comparisons and evaluation, important sampling and sensitivity issues should be carefully considered, as described in previous investigations [e.g., *Li et al., 2007; Marchand et al., 2008; Waliser et al., 2009*].

[5] An issue when performing model-data comparisons of IWC particularly germane to this investigation is the question of which component(s) of the frozen water mass are represented by the retrieval estimates, and how they relate to model representations. We note that, while it is understood that all ice particles are falling under the influence of gravity, cloud particles tend to be quasi-suspended or “floating” and will be referred to “cloud ice” to distinguish them from truly precipitating particles (i.e., snow and graupel). Given the variety of remote sensing instruments, algorithm sensitivities, and model parameterization techniques, significant complexities exist when attempting to carry out model-data comparisons. For example, the CloudSat Cloud Profiling

Radar (CPR) detects nearly all frozen particles as radar reflectivity depends strongly on particle size, while the MLS IWC retrievals are more characteristic of cloud ice alone, owing to difficulties of the microwave radiometer in penetrating thicker clouds.

[6] With the consideration of computational efficiency, most GCMs use simple ice representations that typically divide the total frozen condensate into an amount that remains suspended in the atmosphere and an amount that precipitates. Precipitation is assumed in the model to fall either instantly onto the surface or with sedimentation considered in one time step. The difficulties that arise for comparing CloudSat ice contents with GCMs with simplified ice microphysics are somewhat mitigated for models with a multispecies microphysics scheme, such as the Goddard finite-volume multiscale modeling framework (fvMMF) [Tao and Simpson, 1993; Tao et al., 2003, 2009]. In such models, both suspended and precipitating forms of ice may coexist at any model grid point without instantaneous fallout. Therefore, it is imperative to develop a method to categorize the ice mass estimated by CloudSat into portions of suspended, small particles (cloud ice) and precipitating, large particles (snow and graupel). Such distinction allows one to make more meaningful comparisons to global models with different types of ice representation in observations.

[7] As a preparatory step for making a distinction between cloud versus precipitating IWC, Waliser et al. [2009] filtered out retrievals that were flagged by CloudSat 2B-CLDCLASS algorithm as either exhibiting surface precipitation or the convective cloud types, both of which would be associated with significant amounts of larger falling hydrometeors. The subset of the nonprecipitating and nonconvective (NP and NC) cases was used as a judicious estimate of the suspended ice particles. With the NP and NC constraints applied, the subsampled CloudSat IWC estimates strongly resembles the IWC values estimated by MLS (version 2.2) [Livesey et al., 2007], which is more representative of only the amount of cloud ice. The NP and NC filtering of CloudSat IWC estimates (hereafter referred to as NPC) serves as an initial guide for assessing the cloud ice constituent represented in GCMs. Figure 2 shows the monthly average of total IWC (IWC_{TOTAL}) retrieved by CloudSat Radar-Visible Optical Depth Cloud Water Content retrieval algorithm (2B-CWC-RVOD, v5.1, R04) in August 2006, and the filtered IWC for precipitating or convective (PoC) cases (IWC_{PoC}) and NPC cases (IWC_{NPC}). The values at 350 hPa (Figure 2a) and the zonal mean profile (Figure 2b) suggest that, on a monthly basis, the cloud ice species (IWC_{NPC}) contributes to around 30–60% of the total atmospheric ice mass. However, a filtering based on qualitative information/flags is subject to limitations and caveats. Precipitating and nonprecipitating hydrometeors can coexist at some levels in the column with surface precipitation and/or convective activity. Moreover, not all precipitation in the column will reach surface. Therefore, the PoC cases may still include some cloud ice mass in the precipitating/convective cloud column, while the NPC cases may contain precipitating columns without the presence of surface precipitation owing to evaporation. Moreover, similar subsampling might need to be applied to the model estimates before carrying out model-data comparison.

[8] The present study aims to develop a technique that distinguishes atmospheric ice species based on a quantitative,

microphysical measure, the ice particle size distribution (PSD) provided by the CloudSat algorithm for each IWC retrieval. The new method separates the amount of ice water mass between particles smaller and larger than a selected particle size threshold; the small-sized particles are considered as representative of the suspended cloud ice, while the large ice are deemed precipitating hydrometeors, regardless of the presence of surface precipitation or cloud type. Vertical distributions of cloud ice and precipitating ice mass estimates can therefore be derived in each CloudSat profile. Section 2 describes the CloudSat IWC retrieval algorithm, the methodology for partitioning the ice mass, and the analysis for selecting the appropriate size threshold. Using an ice particle size threshold to distinguish between small ice particles and larger precipitating hydrometeors, the size-partitioned CloudSat IWC estimates are presented in section 3. Sensitivity metrics to the input PSD parameters, and the IWC retrieval algorithm is also discussed. In section 4, the partitioned CloudSat IWC estimates are compared with model representations from the European Centre for Medium-Range Weather Forecasts (ECMWF) model and the fvMMF model. Finally, a summary is provided in section 5 along with a discussion of future development and applications.

2. Data and Methodology

2.1. CloudSat 2B-CWC-RVOD Retrieval Algorithm

[9] CloudSat is one of the five satellites in the A-Train constellation that makes equatorial passes at approximately 01:30 and 13:30 local time. A vertical profile of radar reflectivity factor (Z_e) is measured by the 94 GHz CPR at a vertical resolution of 240 m between the surface and 30 km altitude, during each of the 160 ms measurement intervals. The footprint size is around 1.3 km across track and 1.8 km along track. IWC analyzed in the present study is retrieved from the CloudSat 2B-CWC-RVOD algorithm. This algorithm is a modification of the Radar Only algorithm by Austin et al. [2009] (an earlier version is described by Benedetti et al. [2003]). Only a brief description of the algorithm is provided here, and for details the readers can refer to Austin et al. [2009] and Heymsfield et al. [2008].

[10] The forward model in the retrieval algorithm assumes the ice particles to be spheres with a lognormal particle size distribution (PSD) ($N(D)$); that is,

$$N(D) = \frac{N_T}{\sqrt{2\pi}\sigma_{\log}D} \exp\left[-\frac{\ln^2\left(\frac{D}{D_g}\right)}{2\sigma_{\log}^2}\right] \quad (1)$$

where D represents the diameter of an equivalent mass sphere, D_g is the geometric mean diameter of the ice particles, N_T is the total ice particle number concentration, and σ_{\log} is the distribution width parameter. By integrating the third moment of the PSD over all possible ice particle sizes assuming a constant ice density ($\rho_i = 917 \text{ kg m}^{-3}$), a simple expression can be derived to express the total IWC with the three size distribution parameters (N_T , D_g and σ_{\log}),

$$IWC_{TOTAL} = \int_{D=0}^{D=\infty} \rho_i \frac{\pi}{6} N(D) D^3 dD = \rho_i \frac{\pi}{6} N_T D_g^3 \exp\left(\frac{9}{2}\sigma_{\log}^2\right) \quad (2)$$

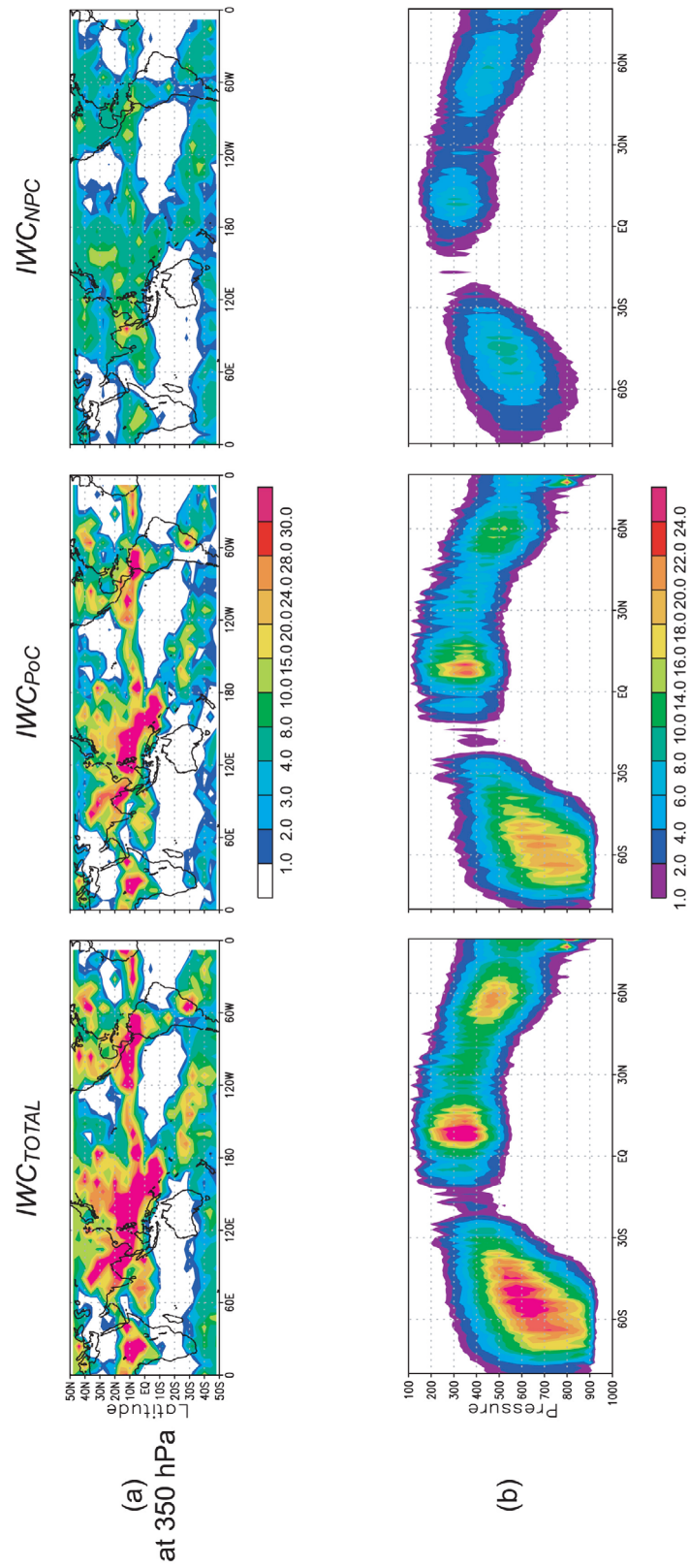


Figure 2. Monthly mean total IWC (IWC_{TOTAL}) and the partitioned IWC based on the filtering technique in the work of Waliser *et al.* [2009] for precipitating or convection cases (IWC_{PoC}), and nonprecipitating and nonconvection cases (IWC_{NPC}) from CloudSat RVOD retrievals in August 2006 (in $mg\ m^{-3}$), with (a) the values at 350 hPa plotted at a $8^\circ \times 4^\circ$ resolution and (b) the zonal altitude mean plotted at a resolution of $4^\circ \times 25$ hPa.

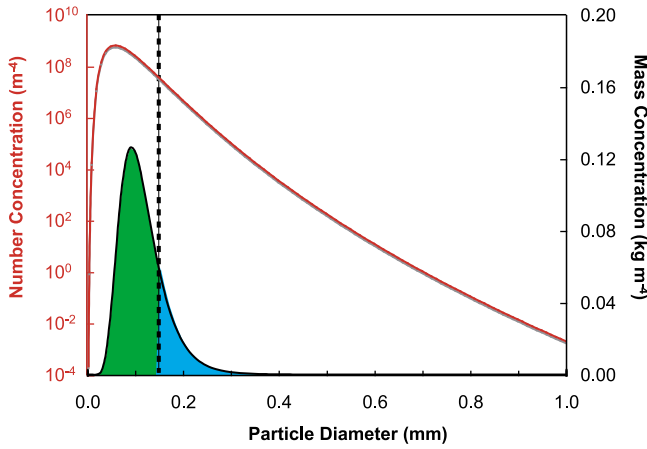


Figure 3. A sample lognormal ice number distribution (red curve; left ordinate in log scale), and the corresponding mass distribution (black curve; right ordinate in linear scale). The dotted line represents the cutoff diameter for IWC partitioning ($D_c = 150 \mu\text{m}$ as an example). The partial integrals of the mass distribution for particles smaller and larger than D_c correspond to $\text{IWC}_{<150}$ (green area) and $\text{IWC}_{>150}$ (blue area), respectively.

[11] The retrieval algorithm obtains an optimized solution by minimizing the difference between the vector of measured reflectivities and the vector of modeled reflectivities derived from the forward model. The optimization iteration is initialized with an a priori PSD, of which the values D_g and σ_{\log} are specified by the temperature dependences obtained from synoptic probe data [Austin *et al.*, 2009], with the temperature information obtained from ECMWF operational analyses. A Z_e -IWC relationship from Liu and Illingworth [2000] is applied to solve for the a priori value of N_T , using the measured reflectivity and a priori values D_g and σ_{\log} as inputs; therefore both temperature and reflectivity are taken into account in determining the a priori PSD. Retrieved IWC and PSD values are obtained by testing for convergence of the iterative solution.

[12] Several ice cloud microphysical retrieval algorithms are compared in the work of Heymsfield *et al.* [2008], using simulated reflectivity and optical depth values based on cloud probe measurements. The mean retrieved-to-measured ratio for IWC from the CloudSat RVOD algorithm is found to be 1.27 ± 0.78 when equivalent radar reflectivity is smaller than -28 dBZ_e . While most of the IWC retrievals are within $\pm 25\%$ of the true value, the algorithm exhibits high bias of over 50% when IWC is less than $\sim 100 \text{ mg m}^{-3}$, with some of the biases related to the potential errors in the measured extinction for small ice crystals in the probe data; therefore the estimated systematic error for IWC is likely $\pm 40\%$ [Heymsfield *et al.*, 2008]. Thin ice clouds are “missed” by CloudSat owing to the instrumental detection limit ($\sim 0.5 \text{ mg m}^{-3}$). On the basis of the comparison with MLS IWC retrievals in the work of Waliser *et al.* [2009] and Wu *et al.* [2009], the amount of thin cirrus ($\text{IWC} < 2 \text{ g m}^{-3}$) missed by CloudSat is estimated to be less than 10% in terms of mass. We also note that in many global models the thin cirrus clouds are not represented or resolved by parameterization. For these global models the IWC estimates presented

in this study can be considered relevant and useful for model evaluation. The upcoming multisensor retrieval data sets [e.g., Delanoë and Hogan, 2010], which take advantages of the different sensitivity of each instrument to particle size and cloud optical depth, are expected to provide better observational constraints for models that are able to represent thin cirrus clouds, and this will be the subject of future studies.

2.2. Partitioning CloudSat IWC on the Basis of PSD

[13] The CloudSat total IWC ($\text{IWC}_{\text{TOTAL}}$) can be partitioned into portions of particles smaller and larger than a specific cutoff diameter (D_c). By representing the ice particles as equivalent spheres with diameter D and constant ice density ρ_i , the partitioned IWC of ice particles larger than D_c ($\text{IWC}_{>D_c}$) is derived by integrating the third moment of the lognormal PSD with D_c as the lower limit,

$$\text{IWC}_{>D_c} = \int_{D=D_c}^{D=\infty} \rho_i \frac{\pi}{6} N(D) D^3 dD \quad (3)$$

[14] The partitioned IWC of ice particles smaller than D_c ($\text{IWC}_{<D_c}$) is computed by subtracting $\text{IWC}_{>D_c}$ from $\text{IWC}_{\text{TOTAL}}$. Figure 3 shows a sample lognormal PSD (red line) and its corresponding mass distribution (black line). An example of cutoff diameter $D_c = 150 \mu\text{m}$ (dotted line) is used to demonstrate the partitioning of $\text{IWC}_{<150}$ (green area) and $\text{IWC}_{>150}$ (blue area).

[15] Selecting the appropriate cutoff diameter for the present methodology is a challenging task, as the size separation between nonprecipitating and precipitating ice particles is not definitive. For example, Morrison and Gettelman [2008] used $200 \mu\text{m}$ as the threshold size (for the particle maximum length) for converting cloud ice to snow by auto-conversion in the GCM bulk cloud scheme. However, on the basis of the analysis of ground-based Doppler radar data, Deng and Mace [2008] found that the mass-weighted fall velocity of cirrus diagnosed from the radar agrees well with sedimentation rate of precipitating ice in the Morrison and Gettelman parameterization, suggesting that all upper tropospheric ice might be considered as precipitation. To identify the likely size separation for floating and precipitating ice species, lights can be shed by investigating the differences of the retrieved PSD between the PoC and NPC filtered cases defined by the surface precipitation and convection flags [Waliser *et al.*, 2009] (also see section 1). Figure 4 shows the temperature (T) dependence of the effective radius (R_e), N_T , and σ_{\log} retrieved from all CloudSat measurements (ALL), and the PoC and NPC cases. The ambient temperature data are taken from collocated ECMWF operational analysis, as in the retrieval algorithm. The mean values and the standard deviations of the three PSD parameters were computed from global observations at 2 K temperature bins. Regional statistics over land and ocean and various latitude bands are subtly different from the global statistics and therefore not shown. The retrieved R_e and σ_{\log} (Figures 4a and 4c) smoothly increases with T ; the values are similar between the PoC and NPC subsets when T is below 240 K. In warmer temperatures the two filtered cases gradually differ: PoC cases show stronger temperature dependence and exhibit larger particle size and PSD width than the NPC cases. The retrieved N_T between

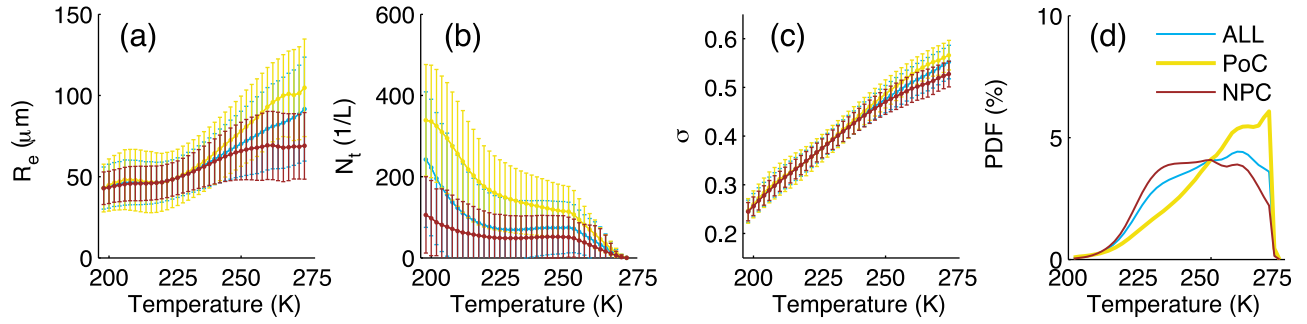


Figure 4. Temperature dependence of (a) effective radius (R_e), (b) ice number concentration, (c) size distribution width parameters (σ_{\log}), and (d) probability density function of in-cloud temperature. The means and the standard deviations are calculated in 2 K temperature bins for all in-cloud cases (ALL, blue line), PoC cases (yellow line), and NPC cases (red line) from CloudSat RVOD retrievals in August 2006.

PoC and NPC cases differ more in lower temperatures and converge when temperature becomes higher, and the PoC cases have higher mean N_T in all temperatures.

[16] To further examine the size separation, the ice mass distributions at six representative temperature bins are plotted in Figure 5 for the PoC (solid yellow line) and NPC (solid red line) subset; each lognormal curve corresponds to the mean value of the PSD parameters calculated in Figure 4 at the selected temperature. The dashed line shows the volume (mass) mean diameter (\overline{D}_v) of each distribution, defined as

$$\overline{D}_v = \left[\frac{6IWC}{\pi \rho_i N_T} \right]^{\frac{1}{3}} \quad (4)$$

[17] For $T < 240$ K (Figures 5a and 5b), the size ranges of the PoC and NPC distribution are narrow (50–200 μm) and mostly overlap, both with the value of \overline{D}_v around 100 μm , smaller than the size in higher-temperature bins. As discussed in section 1, the PoC cases can contain a certain

amount of cloud ice in the column, and most of these small particles in the upper most troposphere are probably the cloud ice species. For $T > 240$ K (Figures 5a–5f), the mean diameter of the NPC cases remains around 100 μm , although the width of the PSD becomes larger in warmer temperatures. Some of the larger particles in the NPC distribution are likely precipitating ice hydrometeors that are not filtered out by the CloudSat surface precipitation flag. The mean diameter of the PoC cases, however, increases with T to as large as 150 μm for $T = 271$ –273 K (Figure 5f), also with strong dispersion.

[18] On the basis of the variation of the mean mass distribution, the size separation of the cloud ice and precipitating ice likely falls between 100 and 200 μm , at least on a global mean basis. This range encompasses the values commonly adopted in GCM cloud parameterization [e.g., Ryan, 2000; Morrison and Gettelman, 2008]. We acknowledge that such size threshold can depend strongly on many variables such as cloud type, updraft velocity, and/or the

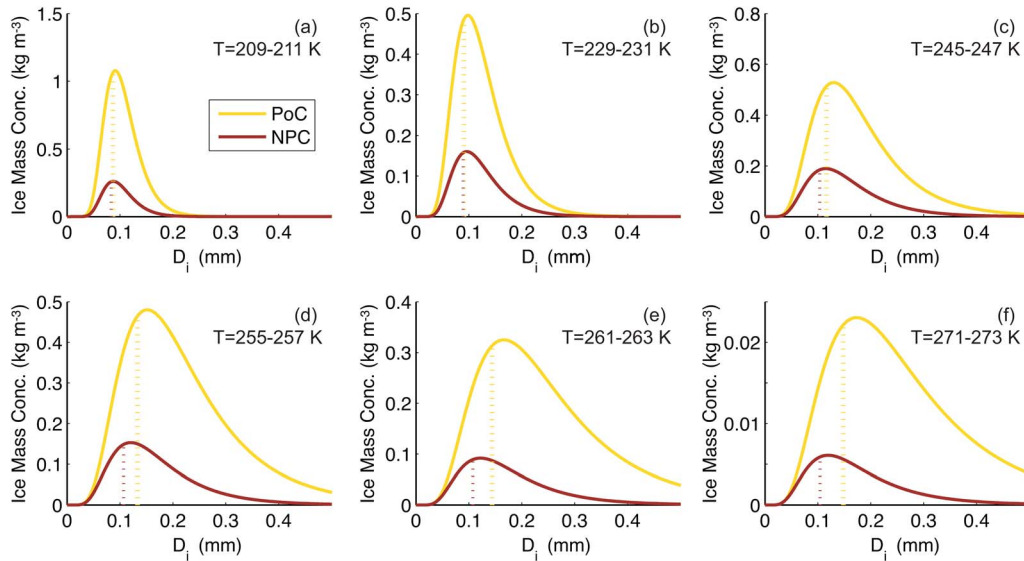


Figure 5. Lognormal ice mass distribution for the CloudSat PoC cases (yellow solid line) and NPC cases (red solid line) with the mean values of the PSD parameters in Figure 4 for temperature bins of (a) 209–211 K, (b) 229–231 K, (c) 245–247 K, (d) 255–257 K, (e) 261–263 K, and (f) 271–273 K. The dashed line shows the volume mean diameter (\overline{D}_v) of each distribution. Note the difference in the vertical axes.

aspect ratio of the ice species, and therefore the threshold can vary drastically among regions and seasons. Detailed investigation will require collocated information from model analysis and the other remotely sensed measurements, and will be the subject of future studies. For the purpose of this study, we aim to provide a first-order estimate of the partitioned CloudSat IWC for the evaluation of the global models. Therefore we report three sets of estimates in section 3, each with a specific, globally constant D_c value, to cover the most possible range of the threshold values identified in the above global statistics and adopted in models. These results, together with those based on the filtering method, represent the lower and upper limits of the partitioned IWC estimates. We also note that, as the technique is under development and is subject to uncertainty associated with the retrieval algorithm, the current results should be taken more qualitatively than quantitatively.

3. Partitioned CloudSat IWC Estimates

3.1. Monthly Mean Size-Partitioned CloudSat IWC Data

[19] The partitioned IWC estimates with $D_c = 100$, 150, and 175 μm are shown and discussed in this section. In Figures 6, 7, 10, 12, and 13 the IWC fields are spatially averaged into 8° longitude by 4° latitude grids in the global maps and 4° latitude by 25 hPa grids in the zonal mean profiles. This is a compromise between a grid size that is comparable to GCM model output, adequate to capture monthly mean variability, and provide adequate samples for each box given CloudSat's nadir-only sampling. We also note that, as the retrieval algorithm does make a priori assumptions, the partitioned IWC presented here represents the interpretation specifically based on the RVOD products. The partitioned IWC will be affected the retrieved PSD parameters and the algorithm employed to retrieve ice PSD parameters; sensitivity analyses to the PSD parameters and the retrieval products are presented in section 3.2. However, we would like to stress that model estimates of ice water path (IWP) vary by two orders of magnitude (e.g., Figure 1), and thus having a quantitative estimate, such as that described here, has significant value despite its shortcomings and uncertainties. Moreover, it prototypes a useful technique that can be elaborated on with the development of increasingly sophisticated instruments and algorithms.

[20] Figure 6 shows the monthly average of the partitioned IWC retrieved by CloudSat RVOD algorithm in August 2006. The mean values at 350 hPa (Figures 6a, 6c, and 6e) and the zonal mean profiles (Figures 6b, 6d, and 6f) for particles larger ($\text{IWC}_{>D_c}$) and smaller ($\text{IWC}_{<D_c}$) than 100, 150, or 175 μm , are displayed. As expected, when a larger cutoff diameter is chosen, the value of the small ice mass increases and that of the large ice mass decreases. In the zonal mean profiles, the CloudSat $\text{IWC}_{\text{TOTAL}}$ and $\text{IWC}_{>D_c}$ in the tropical upper troposphere peaks at 300–400 hPa, while $\text{IWC}_{<D_c}$ peaks at a higher altitude between 250 and 300 hPa. $\text{IWC}_{<D_c}$ fields at 350 hPa with the three cutoff diameter all exhibit high values over areas with frequent and intense convective activities, such as the tropical western Pacific, Central America, and central Africa; the maximum $\text{IWC}_{<D_c}$ is around 6 mg m^{-3} for $D_c = 100 \mu\text{m}$, 13 mg m^{-3} for $D_c = 150 \mu\text{m}$, and 20 mg m^{-3} for $D_c = 175 \mu\text{m}$.

[21] Comparisons can be made between the PSD partitioned IWC (Figure 6) and the filtered IWC based on surface precipitation and convection flags (Figure 2). Despite the different methods, the patterns of the spatial distribution of the partitioned IWC are consistent between the two estimates both vertically and horizontally. The magnitudes of IWC_{NPC} in general lie between $\text{IWC}_{<150}$ and $\text{IWC}_{<175}$ for altitudes below 200 hPa; in the tropics above 200 hPa, the IWC_{NPC} is closest to $\text{IWC}_{<100}$. The zonal mean profiles of the ratio of small ice mass over total ice mass (i.e., $\text{IWC}_{<D_c}/\text{IWC}_{\text{TOTAL}}$) are shown in Figures 7a–7c for the results with the three D_c values. The fraction of small ice mass is in general higher in the upper layers (~ 200 hPa in the Tropics; ~ 350 – 450 hPa in the midlatitudes). The height (temperature) dependences of the ratio are similar among estimates with different cutoff sizes. In the tropical upper troposphere, partitioning with $D_c = 100 \mu\text{m}$ attributes as much as 35% of the total atmospheric ice as small particles. With $D_c = 150$ and $175 \mu\text{m}$, the maximum of this ratio increases to 60%, which is similar to the ratio of IWC_{NPC} over $\text{IWC}_{\text{TOTAL}}$ (Figure 7d). Over the middle and high latitudes around 350–450 hPa, the results indicate that the small ice can contribute to well over 60% of the total ice mass. Figure 8 compares the global monthly mean fraction of the PSD partitioned IWC. As D_c varies from 100 μm to 175 μm , fraction of the small ice species at 350 hPa (Figure 8a) increases from 10% to 37%; the fraction is higher at 250 hPa (Figure 8b), spanning between 13% and 45%. On the basis of the comparison with the filtered IWC, the results with $D_c = 100 \mu\text{m}$ likely represent the lower-end estimate for the fraction of the small ice except for the upper most layers (above 200 hPa).

3.2. Sensitivity of Partitioned CloudSat IWC to the Retrieved PSD Parameters and the Retrieval Algorithm

[22] As the IWC partitioning is based on the retrieved PSD, uncertainties in the PSD parameters would lead to uncertainties in the partitioned ice mass. A second sensitivity is carried out to provide a basic estimation of this uncertainty propagation. In the 2B-CWC-RVOD algorithm (section 2.1), a priori values of the geometric mean diameter (D_g) and the width parameter (σ_{\log}) are empirical functions of temperature (from ECMWF analysis), while the a priori total number concentration (N_T) is determined by both the reflectivity (through the Z_e -IWC relationship) and temperature (through the IWC-PSD relationships with a priori D_g and σ_{\log}). The sensitivity test is constructed by following a procedure analogous to the retrieval algorithm. For all CloudSat IWC retrievals, both the D_g and σ_{\log} are perturbed by 20% of their retrieved values. The corresponding change in N_T is calculated, retaining $\text{IWC}_{\text{TOTAL}}$ at the retrieved value. The perturbed $\text{IWC}_{>D_c}$ is then derived from equation (3) using the perturbed PSD parameters. Note that increasing (decreasing) either D_g or σ_{\log} would flatten (narrow) the PSD and shift the peak of the distribution toward larger (smaller) sizes, leading to an increase (decrease) in the mass fraction of large ice particles. Therefore varying both parameters simultaneously in the same direction represents the extreme cases of the PSD shape biases. The error bars in Figure 8 show the sensitivity of the global monthly mean IWC fractions to a 20% perturbation of both D_g and σ_{\log} , for the three selected values of D_c . For the case of $D_c = 150 \mu\text{m}$, the global mean percentage of small ice particles at 350 hPa

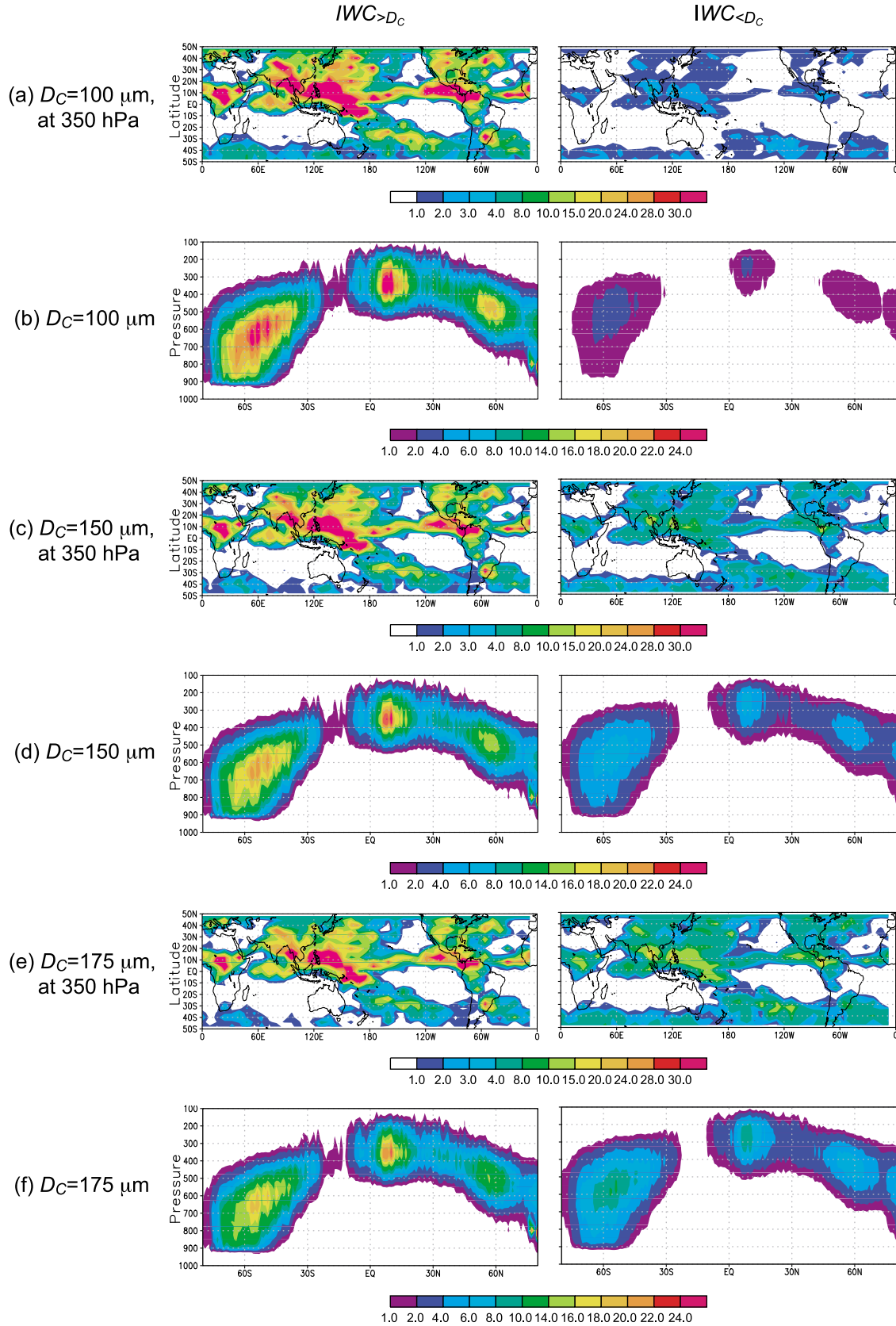


Figure 6. Monthly mean $\text{IWC}_{>D_c}$ and $\text{IWC}_{<D_c}$ from CloudSat RVOD retrievals in August 2006 (in mg m^{-3}): (a) values at 350 hPa plotted at a $8^\circ \times 4^\circ$ resolution, with a cutoff diameter (D_c) of 100 μm ; (b) zonal altitude mean plotted at a resolution of $4^\circ \times 25$ hPa, with $D_c = 100$ μm ; (c and d) similar to Figures 6a and 6b but with $D_c = 150$ μm ; (e and f) similar to Figures 6a and 6b but with $D_c = 175$ μm .

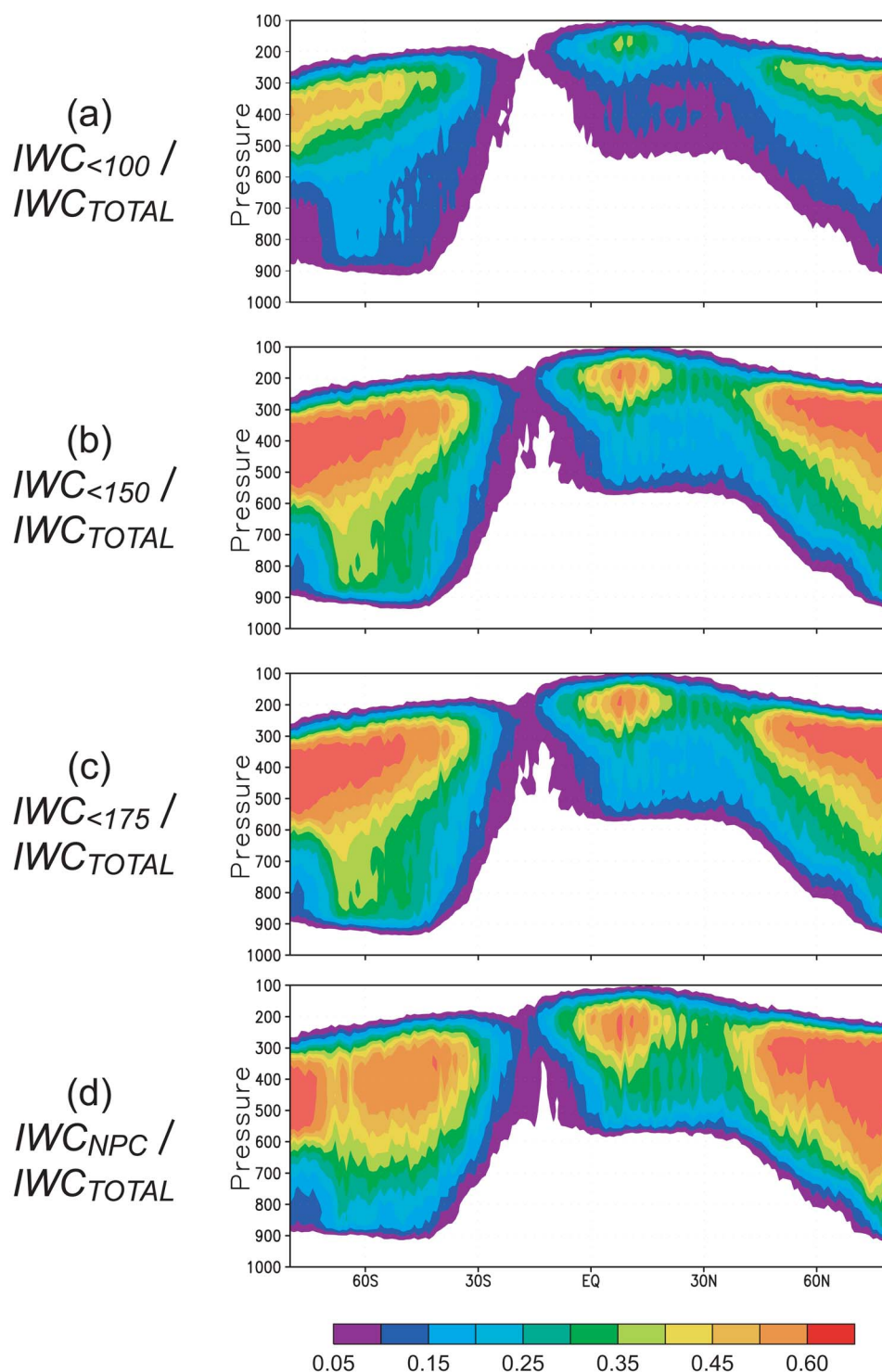


Figure 7. Monthly zonal altitude mean ratio of CloudSat small (nonprecipitating) ice IWC based on (a) $IWC_{<100}$, (b) $IWC_{<150}$, (c) $IWC_{<175}$, and (d) IWC_{NPC} , with respect to IWC_{TOTAL} . Values are computed from CloudSat RVOD retrievals in August 2006.

can increase from 28% to as much as 60% and decrease to 17%; the percentage of the large ice particles also changes accordingly. The sensitivity is higher for larger cut off sizes, and is similar between the 350 hPa and 250 hPa levels.

[23] The partitioned IWC values will also depend on the algorithm employed to retrieve IWC and size distribution

parameters from radar reflectivity. The detail comparisons between CloudSat RVOD and RO retrievals are discussed in the work of *Heymsfield et al.* [2008] and *Austin et al.* [2009]. As the present study is aimed to provide IWC estimates comparable to global model representations, monthly mean values averaged to a grid size similar to a typical GCM

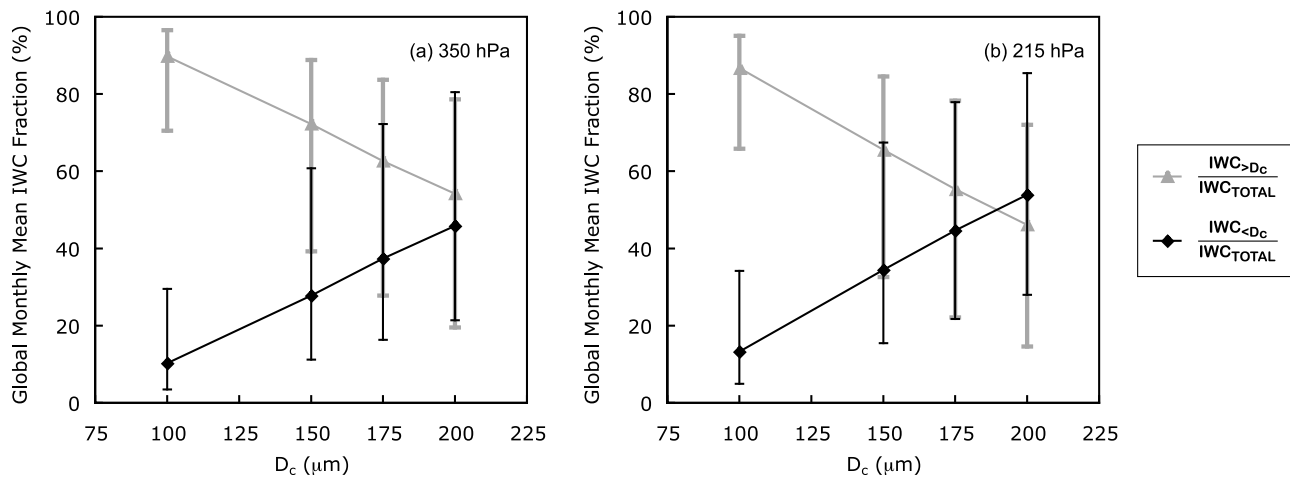


Figure 8. Global monthly mean fractions of partitioned IWC (percent) as a function of the cutoff size (D_c). $IWC_{<D_c}/IWC_{TOTAL}$ (black lines) and $IWC_{>D_c}/IWC_{TOTAL}$ (gray lines) at (a) 350 hPa and (b) 215 hPa from CloudSat RVOD products in August 2006 are shown. The error bars represent the results of perturbing the retrieved size distribution parameters by 20% with the assumption of conserving IWC. Details are provided in section 3.2.

resolution are of interest. Figure 9 compares the total IWC, partitioned IWC with $D_c = 100 \mu\text{m}$, and the effective radius retrieved by the RO and RVOD algorithms. Figure 9 (top) shows 1 day of observation, including all altitudes. The RVOD algorithm retrieves lower IWC than the RO algorithm in many cases; the difference can be as much as 50%. When the same 1 day retrievals are spatially averaged into $8^\circ \times 4^\circ$ grids (Figure 9, middle), the total and partitioned IWC estimates from the two algorithms become closer. Figure 9 (bottom) compares the monthly mean values at an $8^\circ \times 4^\circ$ resolution. The differences are reduced further, indicating that the choice of algorithm will not affect the IWC partitioning results as long as monthly means are considered. The monthly grid-size mean retrieved effective sizes by the two algorithms differ within 10%.

4. Comparisons of Partitioned CloudSat IWC Estimates to Model Representations: ECMWF and fvMMF Models

[24] The size-partitioned CloudSat IWC is compared with the estimates from the ECMWF Integrated Forecast System (IFS CY31R1) and the fvMMF models. Both model estimates have been included in the work of *Waliser et al.* [2009] in the model-data comparisons against the filtered CloudSat IWC subset based on precipitation and convection flags. The ECMWF model is chosen to represent GCMs with a simple ice scheme that provides prognostic outputs only for cloud ice species, while the fvMMF is an example of models with a more sophisticated approach that simulates the more complete budget of both cloud ice and precipitating ice hydrometeors. Brief descriptions of the ice cloud scheme in each model are presented below.

[25] Two kinds of ice crystals are represented in the ECMWF model: “pure ice” and “snow” [*Tiedtke*, 1993]. In the revised scheme, there is no size threshold separating the two species; an explicit autoconversion term that converts ice to snow and a new scheme for ice crystal sedimentation

scheme are applied [*Jung et al.*, 2010]. Immediate fall-out is assumed for snow upon formation, with sublimation and melting in lower levels. The cloud scheme includes processes such as the detrainment of condensates in convection updrafts, collection, accretion, and evaporation. A scheme for homogeneous ice nucleation that allows ice supersaturation to exist in the clear sky is also implemented [*Tompkins et al.*, 2007]. The version of the ECMWF model presented in this study does not have prognostic output for snow, so the total ice estimate represent only the cloud ice species. Also, because of the simpler treatment of microphysics, the model does not calculate the size distribution of ice or snow. Therefore the size partitioning technique cannot be applied on the ECMWF model output.

[26] Figure 10 shows the monthly mean IWC at 350 hPa and the zonal mean profile from the ECMWF IFS CY31R1 for August 2006. At the upper tropospheric levels (above 500 hPa), the pattern of ice mass represented in the ECMWF model matches with the CloudSat estimates for small ice species. The magnitudes of the monthly averaged ECMWF total IWC lie between the CloudSat estimates of $IWC_{<150}$ and $IWC_{<175}$ (Figures 6c–6f) in both the 350 hPa map and the zonal mean profiles. The ECMWF model estimates much higher values of IWC in the lower troposphere in the southern hemispheric high latitudes than the CloudSat estimates of small ice particles (including IWC_{NPC}). This is likely owing to the sedimentation treatment for cloud ice in the model, but we also note that CloudSat IWC retrievals can sometimes be underestimated near melting level in mixed-phase clouds, owing to the liquid-ice partitioning assumption in the algorithm that restricts the IWC values near 0°C [*Austin et al.*, 2009].

[27] The fvMMF employs a single-moment bulk microphysical scheme; the ice parameterization for cloud ice, snow and graupel is similar in many respect to the model discussed in the work of *Rutledge and Hobbs* [1984], with the modification described in the work of *Tao and Simpson* [1993] and *Tao et al.* [2003]. The three species can coexist in each grid, without assuming immediate fallout for the

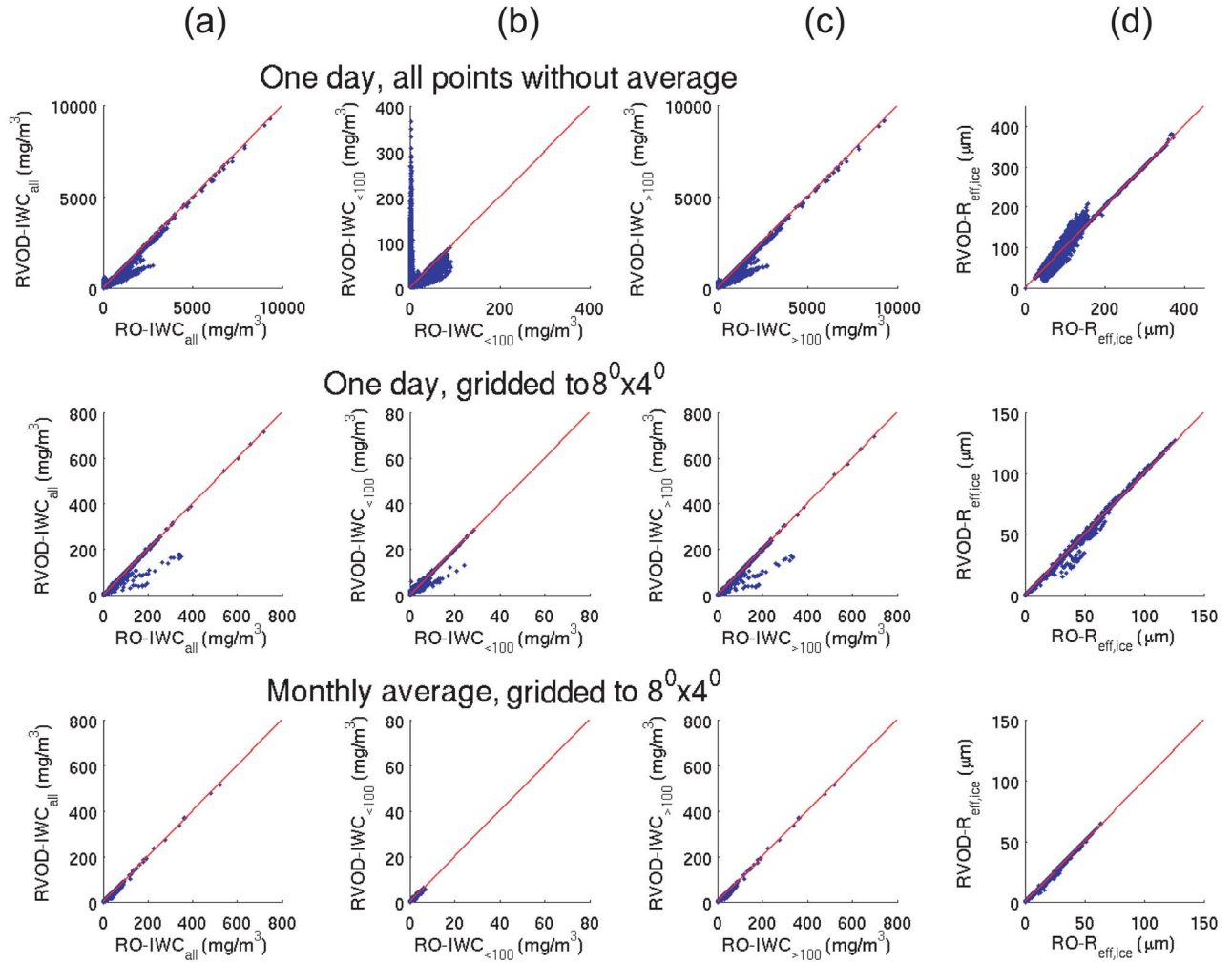


Figure 9. Comparisons between retrievals of CloudSat RO (on the x axis) and RVOD (on the y axis) algorithms for (a) IWC_{TOTAL} , (b) $IWC_{<100}$, (c) $IWC_{>100}$, and (d) R_e . Data (blue dots) from all altitudes on 1 day (15 August 2006) without average (top), on 1 day averaged to a $8^\circ \times 4^\circ$ resolution (middle), and monthly mean averaged to a $8^\circ \times 4^\circ$ resolution (bottom) are shown. The red lines represent the one-to-one line.

precipitating species. The mass budget of each ice species is calculated separately and “saved” as prognostic output. The cloud ice species is represented as a monodispersed quantity with the maximum diameter less than $100 \mu\text{m}$ and the density of ice (917 kg m^{-3}). The total mass of snow and graupel in each grid is fit to an exponential number distribution,

$$Snow_{TOTAL} = \left(\frac{\pi \rho_S N_{oS}}{6} \right) \int_0^\infty D_S^3 e^{-\lambda_S D_S} dD_S = \pi \rho_S N_{oS} \lambda_S^{-4} \quad (5)$$

$$Graupel_{TOTAL} = \left(\frac{\pi \rho_G N_{oG}}{6} \right) \int_0^\infty D_G^3 e^{-\lambda_G D_G} dD_G = \pi \rho_G N_{oG} \lambda_G^{-4} \quad (6)$$

to derive the slope of the distribution (λ), where D represents the diameter of the spherical particle, ρ the particle density and N_o the intercept number concentration, with subscripts “S” for snow and “G” for graupel, respectively ($\rho_S = 100 \text{ kg m}^{-3}$, $\rho_G = 400 \text{ kg m}^{-3}$, $N_{oS} = 16 \times 10^6 \text{ m}^{-4}$,

and $N_{oG} = 4 \times 10^6 \text{ m}^{-4}$). Sample PSDs for snow and graupel in the fvMMF are shown in Figure 11. Since the modeled ice species each follow defined distributions, the ice mass can be readily partitioned by particle size into a contribution from “small” and “large” ice mass with respect to a specified size cutoff. Large particle ice content contributions from snow and graupel in the model are computed by

$$\begin{aligned} Snow_{>D_c} &= \frac{\pi \rho_S N_{oS}}{6} \int_{D=D_c}^\infty D_S^3 e^{-\lambda_S D_S} dD_S \\ &= \frac{\pi \rho_S N_{oS} e^{-\lambda_S D_c}}{6 \lambda_S^4} (D_c^3 \lambda_S^3 + 3 D_c^2 \lambda_S^2 + 6 D_c \lambda_S + 6) \end{aligned} \quad (7)$$

$$\begin{aligned} Graupel_{>D_c} &= \frac{\pi \rho_G N_{oG}}{6} \int_{D=D_c}^\infty D_G^3 e^{-\lambda_G D_G} dD_G \\ &= \frac{\pi \rho_G N_{oG} e^{-\lambda_G D_c}}{6 \lambda_G^4} (D_c^3 \lambda_G^3 + 3 D_c^2 \lambda_G^2 + 6 D_c \lambda_G + 6) \end{aligned} \quad (8)$$

ECMWF CY31R1 Total IWC

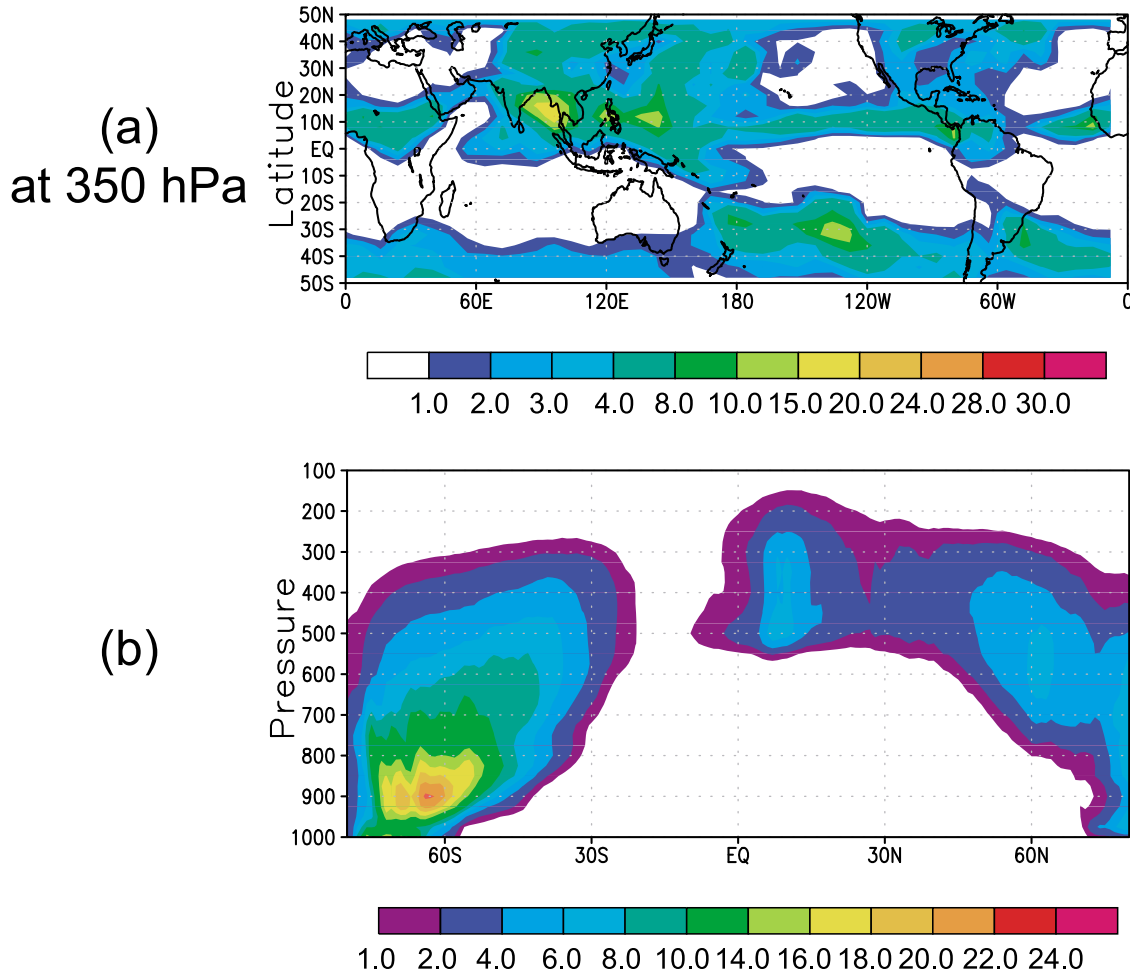


Figure 10. Monthly mean total IWC from ECMWF IFS for August 2006 (in mg m^{-3}): (a) values at 350 hPa and (b) the zonal altitude mean.

[28] The amount of snow and graupel mass considered “small” in the model is computed by subtracting the portion of “large” particle snow and graupel from the total snow and graupel mass, respectively. All of the mass for cloud ice in the model output is attributed to the “small” size category if the chosen cutoff size is larger than $100 \mu\text{m}$. This, coupled with the PSD partitioning technique developed here, provides a basis for model evaluation of IWC with some level of size distribution consideration, which would otherwise be very difficult to achieve.

[29] The total and partitioned CloudSat IWC estimates were used to assess fvMMF model output (Figures 12 and 13). Total IWC from the fvMMF model is partitioned into “small” and “large” categories using the $150 \mu\text{m}$ diameter threshold. Compared to CloudSat estimates (Figure 2), zonal mean $\text{IWC}_{\text{TOTAL}}$ from the fvMMF are overestimated over the areas with high IWC, such as in the Tropics around 350 hPa. The differences are mostly contributed by the overestimation of large ice mass (comparing Figures 6d and 12, middle). Moreover, the maximum $\text{IWC}_{\text{TOTAL}}$ and $\text{IWC}_{>150}$ over the Tropics predicted in the fvMMF is at a lower altitude of

(at 500–600 hPa) than the CloudSat estimates (at 250–400 hPa). However, the zonal mean $\text{IWC}_{<150}$ estimates from the fvMMF is overall smaller than the CloudSat $\text{IWC}_{<150}$, with the altitude of the tropical maximum $\text{IWC}_{<150}$ located at higher levels (at 200–250 hPa) than the CloudSat estimates (at 300–350 hPa). The model–data differences are clearly demonstrated in Figure 13: at 350 hPa the fvMMF $\text{IWC}_{<150}$ fields (Figure 13a) are near zero in the Tropics, while at 215 hPa, the model estimates are close to the CloudSat $\text{IWC}_{<150}$ (Figures 13b and 13c).

[30] We note that the fvMMF model adopts the density of snow and graupel (100 and 400 kg m^{-3} , respectively) to fit the mass into a distribution on the basis of the inverse-exponential number distribution (i.e., equations (5) and (6)), while the CloudSat algorithm assumes the density of ice ($\rho_i = 917 \text{ kg m}^{-3}$) for all particles in the lognormal size distribution (equation (2)). To investigate the effects of the difference in the density assumptions, a sensitivity test was carried out by separating the small and large species on the basis of the mass threshold, instead of the size (volume) cutoff. In other words, in the sensitivity test, the snow or

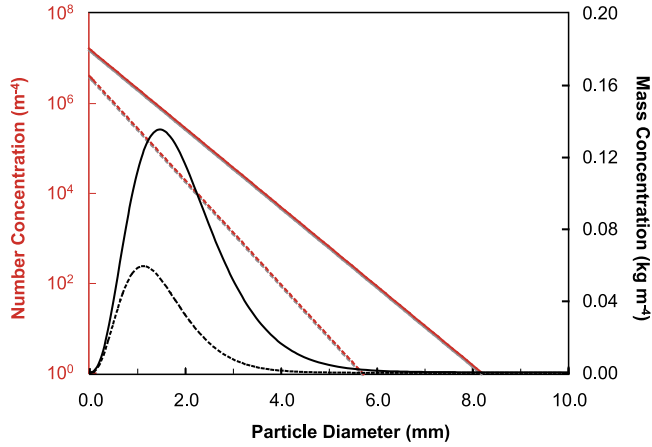


Figure 11. Sample exponential number distributions (red lines; left ordinate in log scale) and the corresponding mass distributions (black curves; right ordinate in linear scale) for snow (solid lines) and graupel (dashed lines) used in the fvMMF. The total mass content for snow and graupel shown in these samples is 0.30 and 0.10 g m^{-3} , respectively. In the fvMMF ice parameterization the cloud ice species is represented as a monodispersed quantity with the maximum diameter less than $100 \mu\text{m}$ (not shown).

graupel particles with a mass smaller than $\rho_i \pi D_c^3 / 6$ (with $D_c = 150 \mu\text{m}$) are categorized as the “small” ice species. The results show the size-partitioned IWC estimates from the model changed by less than 1 mg m^{-3} in the zonal mean. The model estimates of the small ice mass is still much lower than the CloudSat estimates below 300 hPa .

[31] Overall, the comparisons indicate that the fvMMF may overestimate the mass of large, precipitating ice and therefore underestimate the fraction of small ice particles, especially below 300 hPa . The differences between model and retrieved estimates are likely related to the ice deposition velocity assumed in the model. Further investigations can be carried out using the Cloud Resolving Models (CRMs) to confirm the cause of model-data inconsistency in the peak altitudes of the ice content.

5. Summary

[32] Ice clouds, through their radiative and latent heating impacts and associations with precipitation and convective

processes, are tightly connected to the radiation balance, dynamics, and water cycle in the climate system. Reliable climate and weather projections thus depend heavily on appropriate representations of the ice clouds in numerical models. The recent arrival of vertically resolved IWC estimates from satellite sensors, such as CloudSat and MLS, provides crucial observational constraints that can be applied to evaluate and improve the representations of ice clouds in global models. The data-model comparison, however, is a challenging task, as the sensors and the retrieval algorithms can exhibit strong sensitivity to various types of ice hydrometeors, and the complexity and configurations of the ice cloud parameterization in global models also varies considerably.

[33] To better exploit the CloudSat IWC estimates for relevant comparisons against global models’ ice representation, the current study utilizes the ice particle size distribution provided with each CloudSat 2B-CWC-RVOD IWC retrieval to partition the atmospheric ice mass into portions of the small cloud ice and the large, precipitating ice. With the filtering based on CloudSat surface precipitation and convection flags, global statistics of CloudSat-retrieved PSD were collected and analyzed along with the ECMWF temperature data for PoC and NPC filtered cases, to identify relevant range of the partitioning size threshold. Applying an ice particle diameter threshold of 100 , 150 , and $175 \mu\text{m}$ to separate the contributions of the small and large ice particles, the partitioned CloudSat IWC values indicate that 25 – 45% of the global mean total ice mass is from small ice particles, and the contribution can be as much as 60% in the mid-latitudes when a larger cutoff size is chosen. Below 200 hPa , the previous filtering estimates are encompassed by the partitioned IWC estimates with the 150 and $175 \mu\text{m}$ cutoff, while in the upper most layers above 200 hPa , the agreement is closer with the partitioning estimates with the $100 \mu\text{m}$ cutoff. The results are sensitive to the values of the retrieved PSD parameters, while the difference related the choice of IWC retrieval algorithm/products becomes minimal at the typical resolution and time scale (i.e., monthly mean) for model diagnosis. The ECMWF monthly mean total cloud ice analyses showed a close agreement to CloudSat estimates for small ice species in the upper troposphere, with the magnitude between results using $D_c = 150$ and $175 \mu\text{m}$. IWC model output from the fvMMF were partitioned by size in the same fashion as the CloudSat IWC estimates. The comparisons reveal that the fvMMF overestimates the mass of the large ice species in areas of high IWC, subsequently underestimates the contribution from the small particles to the total

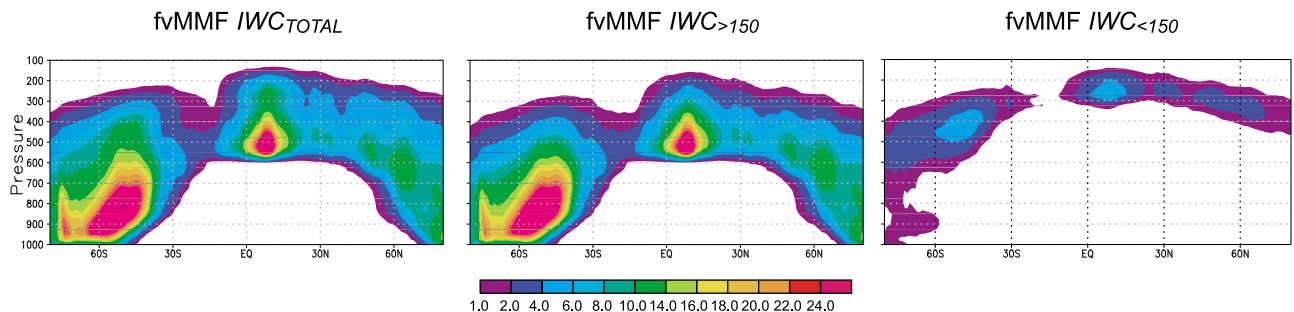


Figure 12. Monthly zonal altitude mean $\text{IWC}_{\text{TOTAL}}$, $\text{IWC}_{>150}$, and $\text{IWC}_{<150}$ from the fvMMF for August 2006 (in mg m^{-3}).

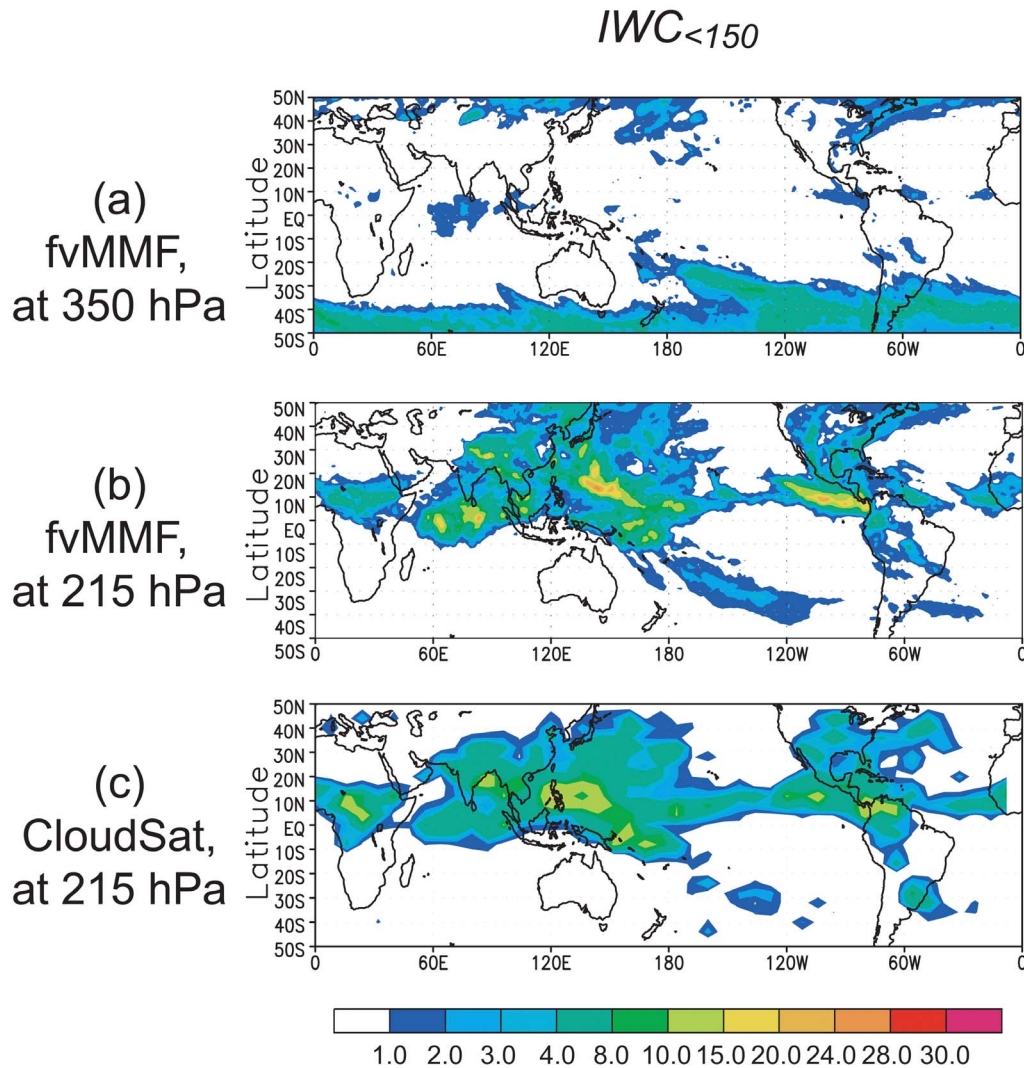


Figure 13. Monthly mean $IWC_{<150}$ for August 2006 (in mg m^{-3}) (a) from the fvMMF at 350 hPa, (b) from the fvMMF at 215 hPa, and (c) from CloudSat estimates at 215 hPa.

ice mass. The altitude of maximum IWC in the tropical upper troposphere is also different between the fvMMF and CloudSat estimates.

[34] The sensitivity measures suggest that the uncertainty of the partitioned IWC estimates can be significant; the current results represent a technique under development and should be taken more qualitatively at this stage. However, the ice water mass simulated by IPCC AR4 GCMs is subject to uncertainties greater than two orders of magnitude (Figure 1). Therefore, any observational estimate, even with an uncertainty factor of two, still provides valuable constraints to the model estimates. We note that the ice mass of the thin cirrus clouds is under detected by CloudSat. Although thin cirrus clouds do not contribute significantly to total atmospheric ice mass, they can still have significant impacts on the hydrological cycle and radiation. Such bias in the CloudSat retrievals can be best evaluated in the future with multi-sensor retrieval data sets [e.g., Delanoë and Hogan, 2010].

[35] The present study points out the importance of quantifying the size separation between nonprecipitating and

precipitating hydrometeors. Future studies will be focusing on the application of collocated model analysis and surface and sounding retrievals to identify the relationships between the size distribution, cloud type, updraft velocity, the thermodynamic environment, and precipitation intensity. A similar concept of PSD-based size partitioning can also be applied to CloudSat-retrieved liquid water content estimates and to studies using the CloudSat radar simulator [Haynes *et al.*, 2007]. The current results can be used in future studies to compare CloudSat IWC to other remotely sensed estimates such as CALIPSO and MLS. The values generated by the partitioning technique can be applied for level-by-level comparisons of cloud ice or liquid, or even mixed phase clouds, between satellite products and analysis estimates. Finally, most GCMs do not include the radiative contribution from precipitating hydrometeors and/or convective cores, and this can result in biases in radiation and subsequent feedbacks to the dynamics and precipitation in the model [e.g., Waliser *et al.*, 2011]. The size-partitioned CloudSat ice and liquid water content data sets can be applied to estimate the impacts

and biases associated with the exclusion of precipitating hydrometeors in the model radiation calculation. With the rich resources from the A-Train satellites and the advance in model parameterization design, the uncertainties and limitation associated with climate simulation and prediction can be reduced as these data are applied to model development and evaluation.

[36] **Acknowledgments.** This research was carried out at the Jet Propulsion Laboratory, California Institute of Technology, under a contract with NASA. It is supported by the NASA CloudSat program. CloudSat data were provided by the NASA CloudSat project through Colorado State University.

References

- Austin, R. T., A. J. Heymsfield, and G. L. Stephens (2009), Retrievals of ice cloud microphysical parameters using the CloudSat millimeter-wave radar and temperature, *J. Geophys. Res.*, **114**, D00A23, doi:10.1029/2008JD010049.
- Baker, M. B. (1997), Cloud physics and climate, *Science*, **276**, 1072–1078, doi:10.1126/science.276.5315.1072.
- Benedetti, A., G. L. Stephens, and J. M. Haynes (2003), Ice cloud microphysics retrievals from millimeter radar and visible optical depth using an estimation theory approach, *J. Geophys. Res.*, **108**(D11), 4335, doi:10.1029/2002JD002693.
- Chen, T., W. B. Rossow, and Y. C. Zhang (2000), Radiative effects of cloud-type variations, *J. Clim.*, **13**, 264–286, doi:10.1175/1520-0442(2000)013<0264:REOCTV>2.0.CO;2.
- Comstock, J. M., T. P. Ackerman, and G. G. Mace (2002), Ground-based lidar and radar remote sensing of tropical cirrus clouds at Nauru Island: Cloud statistics and radiative impacts, *J. Geophys. Res.*, **107**(D23), 4714, doi:10.1029/2002JD002203.
- Delanoë, J., and R. J. Hogan (2010), Combined CloudSat-CALIPSO-MODIS retrievals of the properties of ice clouds, *J. Geophys. Res.*, **115**, D00H29, doi:10.1029/2009JD012346.
- Del Genio, A. D., and W. Kovari (2002), Climatic properties of tropical precipitating convection under varying environmental conditions, *J. Clim.*, **15**, 2597–2615, doi:10.1175/1520-0442(2002)015<2597:CPOTPC>2.0.CO;2.
- Deng, M., and G. G. Mace (2008), Cirrus cloud microphysical properties and air motion statistics using cloud radar Doppler moments: Water content, particle size, and sedimentation relationships, *Geophys. Res. Lett.*, **35**, L17808, doi:10.1029/2008GL035054.
- Fu, Q., and K. N. Liou (1992), On the correlated k-distribution method for radiative transfer in nonhomogeneous atmospheres, *J. Atmos. Sci.*, **49**, 2139–2156, doi:10.1175/1520-0469(1992)049<2139:OTCDMF>2.0.CO;2.
- Hartmann, D. L., and D. Doelling (1991), On the net radiative effectiveness of clouds, *J. Geophys. Res.*, **96**, 869–891, doi:10.1029/90JD02065.
- Hartmann, D. L., and D. A. Short (1980), On the use of Earth radiation budget statistics for studies of clouds and climate, *J. Atmos. Sci.*, **37**, 1233–1250, doi:10.1175/1520-0469(1980)037<1233:OTUOER>2.0.CO;2.
- Hartmann, D. L., M. E. Ockertbell, and M. L. Michelsen (1992), The effect of cloud type on earths energy-balance—Global analysis, *J. Clim.*, **5**, 1281–1304, doi:10.1175/1520-0442(1992)005<1281:TEOCTO>2.0.CO;2.
- Haynes, J. M., R. T. Marchand, Z. Luo, A. Bodas-Sakedo, and G. L. Stephens (2007), A multi-purpose radar simulation package: QuickBeam, *Bull. Am. Meteorol. Soc.*, **88**, 1723–1727, doi:10.1175/BAMS-88-11-1723.
- Heymsfield, A. J., et al. (2008), Testing IWC retrieval methods using radar and ancillary measurements with in situ data, *J. Appl. Meteorol. Climatol.*, **47**, 135–163, doi:10.1175/2007JAMC1606.1.
- Jung, T., et al. (2010), The ECMWF model climate: Recent progress through improved physical parameterizations, *Q. J. R. Meteorol. Soc.*, **136**, 1145–1160, doi:10.1002/qj.634.
- Kahn, B. H., C. K. Liang, A. Eldering, A. Gettelman, Q. Yue, and K. N. Liou (2008), Tropical thin cirrus and relative humidity observed by the Atmospheric Infrared Sounder, *Atmos. Chem. Phys.*, **8**, 1501–1518, doi:10.5194/acp-8-1501-2008.
- Kärcher, B., and J. Ström (2003), The roles of dynamical variability and aerosols in cirrus cloud formation, *Atmos. Chem. Phys.*, **3**, 823–838, doi:10.5194/acp-3-823-2003.
- Kiehl, J. T. (1994), On the observed near cancellation between longwave and shortwave cloud forcing in tropical regions, *J. Clim.*, **7**, 559–565, doi:10.1175/1520-0442(1994)007<0559:OTONCB>2.0.CO;2.
- Krueger, S. K., Q. A. Fu, K. N. Liou, and H. N. S. Chin (1995), Improvements of an ice-phase microphysics parameterization for use in numerical simulations of tropical convection, *J. Appl. Meteorol.*, **34**, 281–287, doi:10.1175/1520-0450-34.1.281.
- Li, J.-L., et al. (2005), Comparisons of EOS MLS cloud ice measurements with ECMWF analyses and GCM simulations: Initial results, *Geophys. Res. Lett.*, **32**, L18710, doi:10.1029/2005GL023788.
- Li, J.-L., J. H. Jiang, D. E. Waliser, and A. M. Tompkins (2007), Assessing consistency between EOS MLS and ECMWF analyzed and forecast estimates of cloud ice, *Geophys. Res. Lett.*, **34**, L08701, doi:10.1029/2006GL029022.
- Lilly, D. K. (1988), Cirrus outflow dynamics, *J. Atmos. Sci.*, **45**, 1594–1605, doi:10.1175/1520-0469(1988)045<1594:COD>2.0.CO;2.
- Lin, B., and W. B. Rossow (1996), Seasonal variation of liquid and ice water path in nonprecipitating clouds over oceans, *J. Clim.*, **9**, 2890–2902, doi:10.1175/1520-0442(1996)009<2890:SVOLAI>2.0.CO;2.
- Liou, K. N. (1976), Absorption, reflection and transmission of solar-radiation in cloudy atmospheres, *J. Atmos. Sci.*, **33**, 798–805, doi:10.1175/1520-0469(1976)033<0798:OTARAT>2.0.CO;2.
- Liu, C.-L., and A. J. Illingworth (2000), Toward more accurate retrievals of ice water content from radar measurements of clouds, *J. Appl. Meteorol.*, **39**, 1130–1146, doi:10.1175/1520-0450(2000)039<1130:TMAROI>2.0.CO;2.
- Livesey, N. J., et al. (2007), Earth Observing System (EOS) Aura Microwave Limb Sounder (MLS) Version 2.2 Level 2 Data Quality and Description, *Rep. D-33509*, 115 pp., Jet Propul. Lab, Pasadena, Calif.
- Luo, Z., and W. B. Rossow (2004), Characterizing tropical cirrus life cycle, evolution, and interaction with upper-tropospheric water vapor using Lagrangian trajectory analysis of satellite observations, *J. Clim.*, **17**, 4541–4563, doi:10.1175/3222.1.
- Lynch, D. K., K. Sassen, D. O. Starr, and G. L. Stephens (Eds.) (2002), *Cirrus*, pp. 449–455, Oxford Univ. Press, New York.
- Marchand, R., G. G. Mace, T. Ackerman, and G. Stephens (2008), Hydrometeor detection using Cloudsat—An Earth-orbiting 94-GHz cloud radar, *J. Atmos. Oceanic Technol.*, **25**, 519–533, doi:10.1175/2007JTECHA1006.1.
- McFarquhar, G. M., and A. J. Heymsfield (1996), Microphysical characteristics of three anvils sampled during the central equatorial Pacific experiment, *J. Atmos. Sci.*, **53**, 2401–2423, doi:10.1175/1520-0469(1996)053<2401:MCOTAS>2.0.CO;2.
- McFarquhar, G. M., A. J. Heymsfield, J. Spinhirne, and B. Hart (2000), Thin and subvisual tropopause tropical cirrus: Observations and radiative impacts, *J. Atmos. Sci.*, **57**, 1841–1853, doi:10.1175/1520-0469(2000)057<1841:TASTTC>2.0.CO;2.
- Miller, R. L. (1997), Tropical thermostats and low cloud cover, *J. Clim.*, **10**, 409–440, doi:10.1175/1520-0442(1997)010<0409:TTALCC>2.0.CO;2.
- Morrison, H., and A. Gettelman (2008), A new two-moment bulk stratiform cloud microphysical scheme in the Community Atmosphere Model (CAM3), part I: Description and numerical tests, *J. Clim.*, **21**, 3642–3659, doi:10.1175/2008JCLI2105.1.
- Ramanathan, V., and W. Collins (1991), Thermodynamic regulation of ocean warming by cirrus clouds deduced from observations of the 1987 El Niño, *Nature*, **351**, 27–32, doi:10.1038/351027a0.
- Ramanathan, V., R. D. Cess, E. F. Harrison, P. Minnis, B. R. Barkstrom, E. Ahmad, and D. Hartmann (1989), Cloud-radiative forcing and climate—Results from the Earth Radiation Budget Experiment, *Science*, **243**, 57–63, doi:10.1126/science.243.4887.57.
- Randall, D. A., and S. Tjemkes (1991), Clouds, the Earth's radiation budget, and the hydrologic cycle, *Global Planet. Change*, **4**, 3–9, doi:10.1016/0921-8181(91)90063-3.
- Rossow, W. B., and R. A. Schiffer (1999), Advances in understanding clouds from ISCCP, *Bull. Am. Meteorol. Soc.*, **80**, 2261–2287, doi:10.1175/1520-0477(1999)080<2261:AIUCFI>2.0.CO;2.
- Rutledge, S., and P. V. Hobbs (1984), The mesoscale and microscale structure and organization of clouds and precipitation in midlatitude cyclone XII: A diagnostic modeling study of precipitation development in narrow cold-frontal rain bands, *J. Atmos. Sci.*, **41**, 2949–2972, doi:10.1175/1520-0469(1984)041<2949:TMAMSA>2.0.CO;2.
- Ryan, B. F. (2000), A bulk parameterization of the ice particle size distribution and the optical properties in ice clouds, *J. Atmos. Sci.*, **57**, 1436–1451, doi:10.1175/1520-0469(2000)057<1436:ABPOTI>2.0.CO;2.
- Stephens, G. (2005), Cloud feedbacks in the climate system: A critical review, *J. Clim.*, **18**, 237–273, doi:10.1175/JCLI-3243.1.
- Stephens, G., G. G. Campbell, and T. H. Vonderhaar (1981), Earth radiation budgets, *J. Geophys. Res.*, **86**, 9739–9760, doi:10.1029/JC086iC10p09739.

- Stephens, G., et al. (2002), The CloudSat mission and the A-Train—A new dimension of space-based observations of clouds and precipitation, *Bull. Am. Meteorol. Soc.*, **83**, 1771–1790, doi:10.1175/BAMS-83-12-1771.
- Tao, W. K., and J. Simpson (1993), Goddard cumulus ensemble model. Part I: Model description, *Terr. Atmos. Oceanic Sci.*, **4**, 35–72.
- Tao, W. K., et al. (2003), Microphysics, radiation and surface processes in the Goddard Cumulus Ensemble (GCE) model, *Meteorol. Atmos. Phys.*, **82**, 97–137, doi:10.1007/s00703-001-0594-7.
- Tao, W. K., et al. (2009), A multiscale modeling system: Developments, applications, and critical issues, *Bull. Am. Meteorol. Soc.*, **90**, 515–534, doi:10.1175/2008BAMS2542.1.
- Tiedtke, M. (1993), Representation of clouds in large-scale models, *Mon. Weather Rev.*, **121**, 3040–3061, doi:10.1175/1520-0493(1993)121<3040:ROCILS>2.0.CO;2.
- Tompkins, A. M., K. Gierens, and G. Rädcl (2007), Ice supersaturation in the ECMWF Integrated Forecast System, *Q. J. R. Meteorol. Soc.*, **133**, 53–63, doi:10.1002/qj.14.
- Waliser, D. E., et al. (2009), Cloud ice: A climate model challenge with signs and expectations of progress, *J. Geophys. Res.*, **114**, D00A21, doi:10.1029/2008JD010015.
- Waliser, D. E., J.-L. F. Li, T. S. L’Ecuyer, and W.-T. Chen (2011), The impact of precipitating ice and snow on the radiation balance in global climate models, *Geophys. Res. Lett.*, **38**, L06802, doi:10.1029/2010GL046478.
- Wu, D. L., J. H. Jiang, and C. P. Davis (2006), EOS MLS cloud ice measurements and cloudy-sky radiative transfer model, *IEEE Trans. Geosci. Remote Sens.*, **44**, 1156–1165, doi:10.1109/TGRS.2006.869994.
- Wu, D. L., et al. (2009), Comparisons of global cloud ice from MLS, CloudSat, and correlative data sets, *J. Geophys. Res.*, **114**, D00A24, doi:10.1029/2008JD009946.
- Zelinka, M. D., and D. L. Hartmann (2010), Why is longwave cloud feedback positive?, *J. Geophys. Res.*, **115**, D16117, doi:10.1029/2010JD013817.

W.-T. Chen, J. H. Jiang, J.-L. F. Li, D. E. Waliser, and C. P. Woods, Jet Propulsion Laboratory, California Institute of Technology, 4800 Oak Grove Dr., Pasadena, CA 91109, USA. (annechen@caltech.edu)

J.-D. Chern and W.-K. Tao, NASA Goddard Space Flight Center, Code 613.1, Greenbelt, MD 20771, USA.

A. M. Tompkins, Abdus Salam International Centre for Theoretical Physics, Strada Costiera 11, I-34152 Trieste, Italy.